LAWRENCE
LIVERMORE
NATIONAL
LABORATORY

UCRL-CONF-216755

In-Situ Observations of Phase Transformations During Welding of 1045 Steel using Spatially Resolved and Time Resolved X-Ray Diffraction

J. Elmer, T. Palmer, T. DebRoy

November 2, 2005

Modeling of Casting, Welding and Advanced Solidification Processes XI
Opio, France
May 28, 2006 through June 2, 2006

Disclaimer

In-Situ Observations of Phase Transformations During Welding of 1045 Steel using Spatially Resolved and Time Resolved X-Ray Diffraction

J. W. Elmer [1], T. A. Palmer[1], and T. DebRoy[2]

[1]Lawrence Livermore National Laboratory, Livermore, California, USA

[2]The Pennsylvania State University, University Park, Pennsylvania, USA

Keywords: Synchrotron radiation, austenite, ferrite, martensite, bainite, kinetics

Abstract

Synchrotron-based methods have been developed at Lawrence Livermore National Laboratory (LLNL) for the direct observation of microstructure evolution during welding. These techniques, known as spatially resolved (SRXRD) and time resolved (TRXRD) x-ray diffraction, allow in-situ experiments to be performed during welding and provide direct observations of high temperature phases that form under the intense thermal cycles that occur. This paper presents observations of microstructural evolution that occur during the welding of a medium carbon AISI 1045 steel, using SRXRD to map the phases that are present during welding, and TRXRD to dynamically observe transformations during rapid heating and cooling. SRXRD was further used to determine the influence of welding heat input on the size of the high temperature austenite region, and the time required to completely homogenize this region during welding. These data can be used to determine the kinetics of phase transformations under the steep thermal gradients of welds, as well as benchmark and verify phase transformation models.

Introduction

Synchrotron radiation, which is many orders of magnitude more intense than conventional x-rays, can be passed between an array of powerful magnetic poles called a wiggler, to further increase the x-ray brightness [1]. The resulting intense, highly collimated radiation can be used to probe atomic structures in time scales of milliseconds and with sub-mm resolution, making real-time observations of phase transformations during welding possible [2]. Techniques have been developed using synchrotron radiation to provide information about welding-induced phase transformations that cannot be obtained by conventional characterization methods which are limited by their inability to provide direct information about the weld microstructure as it evolves.

In the spatially resolved x-ray diffraction (SRXRD) technique, diffraction patterns are acquired at discreet locations along a linear scan beginning in the weld fusion zone and proceed through the weld Heat Affected Zone (HAZ) and into the base metal. The results allow the phase transformations occurring over a range of locations in the weld HAZ to be monitored during steady state welding conditions. In the time resolved x-ray diffraction (TRXRD) technique, x-ray diffraction patterns are again acquired in real time, but they are acquired at very short time intervals during welding at a single weld location during a transient spot weld, again using sub-mm sized beams. TRXRD allows the evolution of a phase transformation to be monitored with high temporal resolution (10 to 100 ms) during rapid weld heating and cooling conditions.

Over the past several years both techniques have been used to study phase transformations in steels [2-6], welding filler metals [7, 8], and other alloys [9-13]. These data have formed the basis for the development of kinetic models used to predict weld phase transformations under different welding conditions [14-17]. This article provides a brief overview of results for 1045 steel which undergoes an $\alpha \rightarrow \gamma \rightarrow \alpha$ phase transformation sequence during welding, and creates bainitic and martensitic microstructures during rapid weld cooling.

Materials and Experimental Procedures

Gas tungsten arc (GTA) welds were made on cylindrical bar samples of the 1045 steel while performing in-situ observations of the phase transformations. The steel contains 0.46 C, 0.85 Mn, and 0.27 Si wt. percent, and its heat treatment is such that the base metal microstructure contains allotriomorphic ferrite (12%) and pearlite (88%) [4-6]. The prior austenite grain size is 92.8 μm, and the size of the allotriomorphic grain boundary ferrite phase is 15 μm to 20 μm wide on average, with some patches reaching 30 μm or more in places [4-6].

The GTA welds were made on the 1045 steel at power levels between 1 and 4kW, and at a travel speed of either 0.6 mm/s (SRXRD) [4-6], or under stationary spot welding conditions (TRXRD) [18]. The welding parameters produced fusion zones approximately 10 mm wide and 5 mm deep in both cases. The welds were made on 10.2 cm diameter cylindrical bars inside an environmentally sealed chamber (see Fig. 1) that was pumped down to vacuum conditions before backfilling with high purity helium prior to welding. The helium prevented atmospheric contamination of the weld, and minimized attenuation of the x-ray beam. Details of these and similar welding experiments on carbon-manganese steels are reported elsewhere [3-6, 18].

The major components of the experimental setup used for the SRXRD and TRXRD experiments are indicated in Fig 1. In each experiment, the x-ray beam passes through a monochromator before passing through a tungsten pinhole. This produces a monoenergetic and sub-millimeter sized beam, which impinges on the sample at a given location. In the SRXRD experiment (shown), discreet HAZ locations are analyzed along the path perpendicular to the weld direction with 250 μm precision. The TRXRD setup is identical, but welds are made on a stationary bar, and only a single location is probed during the transient spot weld.

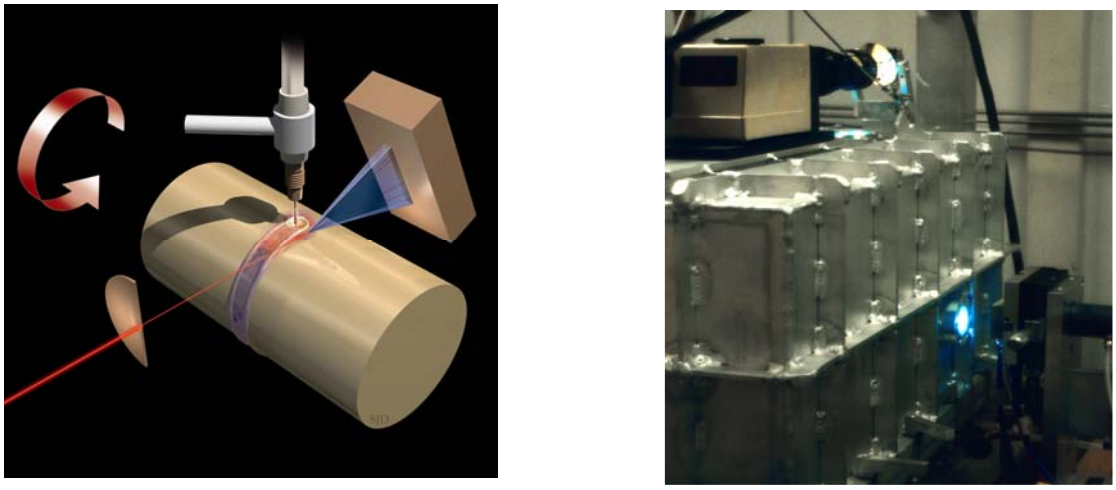

Figure 1. a) Schematic diagram of the SRXRD experimental setup, and b) Environmental chamber in the x-ray beam hutch during an experiment.

The in-situ x-ray diffraction experiments discussed in this paper were performed using the 31-pole wiggler beam line, BL 10-2 at Stanford Synchrotron Radiation Laboratory (SSRL) with

SPEAR (Stanford Positron-Electron Accumulation Ring) operating at an electron energy of 3.0 GeV and an injection current of ~100 mA. Fig. 1 shows the experimental setup where the focused monochromatic synchrotron x-ray beam is passed through a tungsten pinhole, 250 μm (SRXRD) or 540 μm (TRXRD), to render a sub-millimeter beam on the sample at an incident angle of ~25°. This setup yields a beam flux on the sample of $\sim 10^{12}$ photons/s, which was determined experimentally using an ion chamber immediately downstream from the pinhole (not shown). A photon energy of 12.0 keV ($\lambda = 0.1033$ nm) was chosen to facilitate phase identification and to be far enough in energy above the Fe K-edge (7.112 keV) to minimize the background contribution due to Fe K-fluorescence from the steel samples.

The x-ray diffraction patterns were recorded using a 50 mm long 2048 element position sensitive Si photodiode array detector. The array was mounted on a dual-stage water cooled Peltier effect thermoelectric cooler at a location approximately 10 cm behind the weld to cover a 2θ range from 22° to 52°. This 2θ range was optimized to contain a total of six diffraction peaks, three from the bcc phase (α-Fe) and three from the fcc phase (γ-Fe). Calibration of the x-ray diffraction patterns was performed using a thin niobium foil, which has a well characterized bcc crystal structure. Other details about the experimental setup can be found in previous publications; see for example references [3, 14] for SRXRD and [11, 18] for TRXRD..

Modeling and Analysis

Diffraction Peak Analysis The x-ray diffraction patterns gathered during the welding experiments were analyzed to determine the phases present and the semi-quantitative volume fractions of each phase. This analysis measured the integrated intensity of the peaks in each diffraction pattern using a sum of one or more Gaussian peak profile fitting functions [9, 14]. The area and FWHM values of the fitted peaks were then determined using an automated curve-fitting routine developed in Igor Pro®, Version 4.0. The raw integrated intensities of the diffraction peaks were then converted into relative phase intensities. This conversion is based on the effects of a number of factors on the resulting intensity of a given peak. In this method, the peak area or integrated intensity of each peak is measured and then converted to relative fraction of each phase by considering the crystal structure, the Lorentz polarization factor, and the temperature. The overall methodology used is described elsewhere [14].

Thermal Modeling Direct measurement of weld temperatures is very difficult, particularly during in situ experiments. To overcome this difficulty, weld thermal cycles were calculated, instead. These calculations were used to determine the weld temperature as a function of position (SRXRD), and as a function of time at a given position (TRXRD). The weld model was developed by the Pennsylvania State University, and utilizes a 3D numerical heat transfer and fluid flow code that was created specifically for welds [19, 20]. The model solves the equations of conservation of mass, momentum and energy in three-dimensional form to determine the size and shape of the liquid weld pool. In the SRXRD experiments, the thermal profile in the steady state weld pool and in the HAZ was determined for the for the quasi steady state welding condition. In the TRXRD experiments, transient thermal profiles arecalculated as a function of time and position for spot welding conditions using the mathematical formulation discussed in reference [16]. Applications of the coupled thermal-fluids model for the steady state welds used for SRXRD are discussed in references [13-15, 17], while the application of to the transient welds used in the TRXRD experiments are discussed in references [11, 18].

Phase Equilibria Thermocalc® was used to calculate the phase diagram, and thus the phase transformation sequence for the 1045 steel alloy [21]. The chemical effects of Fe, C, Si, Mn, Ni and Cr on the liquid, ferrite, austenite, and cementite phase fields, were considered and the

results indicate that the equilibrium starting microstructure will consist of a mixture of ferrite and transform to austenite when the A1 temperature of 712ºC is reached. Complete transformation to austenite will occur at the A3 temperature of 765ºC, and this austenite will remain stable until melting begins to occur at 1410ºC. The transformations that occur during heating will be reversed during cooling. However, kinetic limitations may affect the predicted start and completion temperatures of the phase transformations, and the formation of non-equilibrium phases such as bainite and/or martensite may occur at high cooling rates. The determination of the bainite and martensite start temperatures are discussed elsewhere [18].

Results and Discussion

SRXRD Phase Mapping Transformations were observed in the HAZ of each of the 1045 steel during welding using SRXRD phase mapping. To do this, diffraction patterns were acquired in rows perpendicular to the direction of the weld. Each diffraction pattern was acquired in 0.25 mm increments, and each row of data contained more than 30 individual x-ray patterns. More than 20 rows of data were required to complete a phase map which contained more than 600 individual diffraction patterns in the weld HAZ. The x-ray diffraction peaks were analyzed using peak area based methods specifically in the two phase regions, to estimate the relative volume fractions of α and γ at each location in the HAZ using the technique detailed in reference [14]. The resulting data contains semi-quantitative information about the relative amounts of ferrite and austenite that exist in the HAZ during welding, and the results are shown in Fig 2 for a weld made at an input power of 2.4 kW at a travel speed of 0.6 mm/s [4].

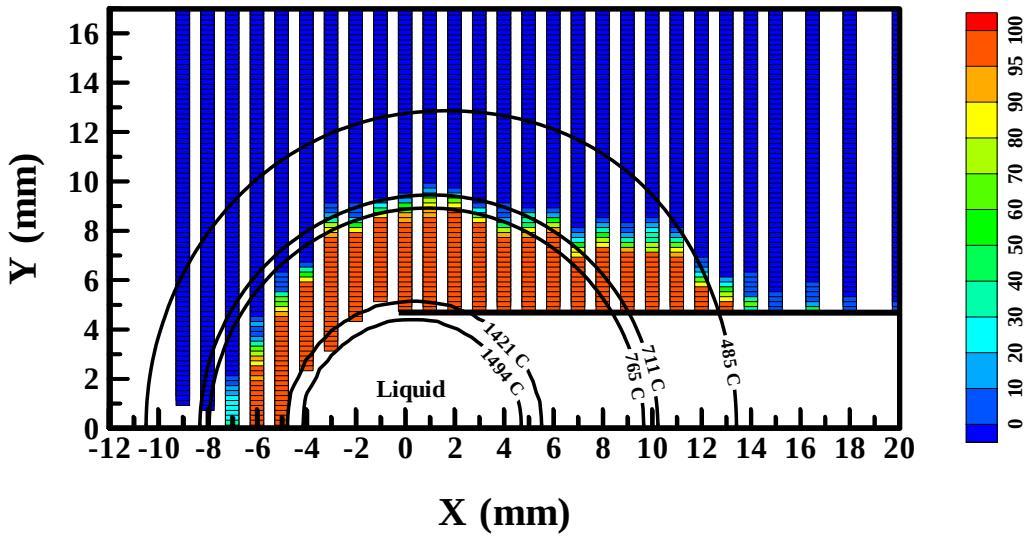

Figure 2: SRXRD semi-quantitative map showing the volume fraction of austenite (red) in the 1045 steel HAZ. The scale indicates the amount of austenite (0-100%), and the calculated isotherms are shown for the liquidus, solidus, A3, A1, and bainite start temperatures [18].

The weld isotherms, calculated using the coupled thermal fluids weld model discussed previously, are superimposed over the SRXRD data. The locations of the α and γ phases are plotted with 250 μm precision perpendicular to the welding direction and 500 μm parallel to the welding direction. In the plot, the shading indicates the γ fraction, which varies from 0% (blue) to 100% (red). The individual SRXRD line scans were made perpendicular to the welding direction, and show a variation in γ from 0 to 100% over a narrow region approximately 1.0 to 1.6 mm wide. These regions indicate where the α→γ phase transformation is taking place in the weld HAZ.

It is clear from this figure that a large γ phase field surrounds the weld pool, and that this phase field is expanded on the trailing side of the weld with respect to the A3 isotherm (765°C). It is apparent from the location of the γ phase field, that the completion of the α→γ phase transformation is shifted to higher temperatures on heating and to lower temperatures on cooling relative to the A3 temperature. Differences between the measured and calculated location of the γ phase field is evidence of the non-equilibrium conditions that exist during welding. The results indicate that superheating is required to completely transform the microstructure to γ on heating, and that undercooling is required to initiate the transformation to α on cooling [4]. The lag required to complete the transformation to γ on heating is displaced further from the A3 isotherm at locations closer to the weld centerline where the heating rates are the highest. This shows that the amount of superheating required for the α→γ transformation varies with heating rate. During cooling, the region closest to the fusion zone requires considerable undercooling prior to measurable amounts of transformation.

Affect of Heat Input on Austenitization. Variations in the size of the observed γ phase field occur as a result of changes in the weld heat input, and these effects were studied in the 1045 steel using SRXRD for welding heat inputs between 1000 and 4000 W at a travel speed of 0.6 mm/s [5]. The locations of the γ, α+γ, and α phase regions measured in the SRXRD scan made at a weld input power of 1984 W are shown Fig. 3a. The calculated isotherms for the liquidus, solidus, A3, and A1 temperatures, and the locations of the HAZ microstructural features observed in the post-weld metallography are also shown for this heat input.

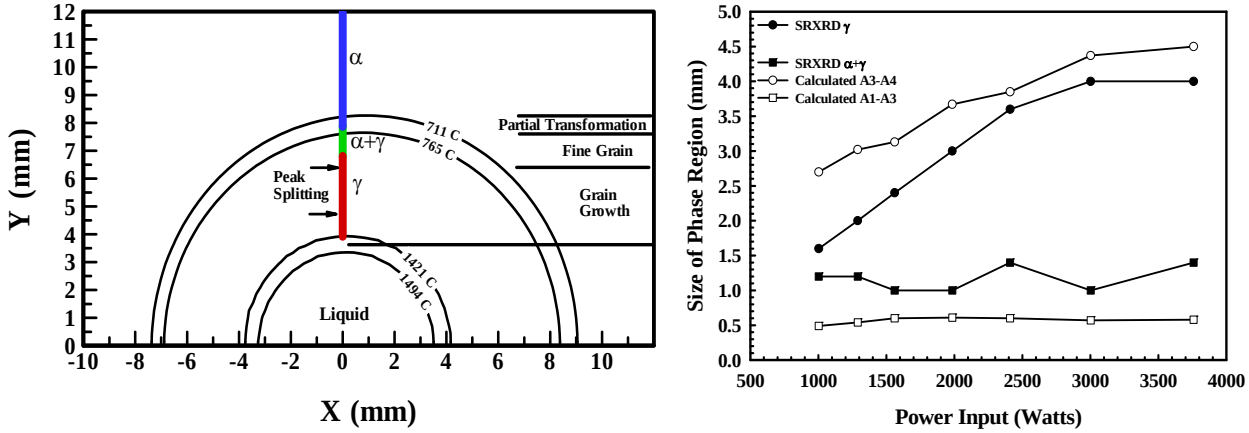

Figure 3: a) Calculated isotherms, SRXRD experimental observations, and the widths of the HAZ regions for an 1984 W GTA weld. b) SRXRD measured sizes of the phase regions, and calculated values based on equilibrium transformation temperatures as a function of heat input.

The widths of the γ and α+γ phase regions over the range of input powers were determined and are plotted in Fig. 3b (solid symbols). These values are then compared with the calculated sizes of these phase regions, based on thermodynamic considerations (open symbols). The variations between the calculated and experimental sizes of the γ phase region differ over the range of input powers investigated here. These differences are largest at the lower input powers where the temperature gradients for the weld input powers are highest. At the higher input powers, the experimental and calculated sizes of the γ phase region are similar. The size of the α+γ phase region remains fairly constant over the range of input powers, but the measured width of the α+γ phase region is always larger than the calculate value.

Homogenization of Austenite. Within the austenite region, the austenite phase was observed form inhomogeneously, which resulted in the creation of two distinct sets of x-ray diffraction

peaks for all of the input powers investigated. The splitting occurs over a finite region of the austenite phase field as indicated by the two arrows in Fig. 3a for the 1984 W weld [5, 6]. When the peaks split, a higher d-spacing (lower 2θ) austenite, γ_2, begins to form on the initial austenite, γ_1. Fig. 4a shows one of these split peaks for the fcc(111) reflection at a location 5.2 mm from the weld centerline. The splitting is first observed near a calculated temperature of 884ºC, and the larger γ_2 lattice parameter is the result of higher concentrations of carbon and manganese. The primary source of these alloying elements is the undissolved cementite laths, which begin to dissolve into the austenite at elevated temperatures. Initially, the split between the γ_1 and γ_2 peaks is rather small, since γ_2 first begins to form from the γ_1 located within the pearlite colonies. With increasing temperatures, the amount of peak splitting increases as both the carbon and manganese from the cementite diffuse into the γ_2 constituent. The amount of peak splitting reaches a maximum as the temperatures approach 1243ºC, which is assumed to correspond to the completion of the cementite dissolution [5, 6]. With further increases in temperature, the amount of splitting decreases until only a single peak is observed at locations near the fusion zone boundary when the austenite phase (γ) reaches completion as the diffusion of the alloying elements creates a single chemically homogenous austenite phase.

The peak splitting behavior providence for the mechanism for the transformation of the base metal microstructure and the homogenization of the resulting austenite phase during welding. This mechanism is schematically shown in Fig. 4b. In the initial stages (a), ferrite in the pearlite colonies and allotriomorphic ferrite regions which surround them in the base metal is transformed into austenite, γ_1, (b). Because of the rapid heating cycles experienced in the weld HAZ, the cementite laths, which are originally a part of the pearlite colonies, do not completely dissolve before the ferrite in the microstructure is completely consumed above the A3 temperature. These cementite laths begin to dissolve with continued heating, introducing C and Mn into the austenite and causing a second, more highly alloyed austenite constituent, γ_2, to appear (c). As the heating continues, these alloying elements, which originated in the cementite laths, continue to diffuse into the less highly alloyed γ_1 constituent. At temperatures of approximately 1300ºC and above, the chemical composition of the austenite becomes homogenized (d).

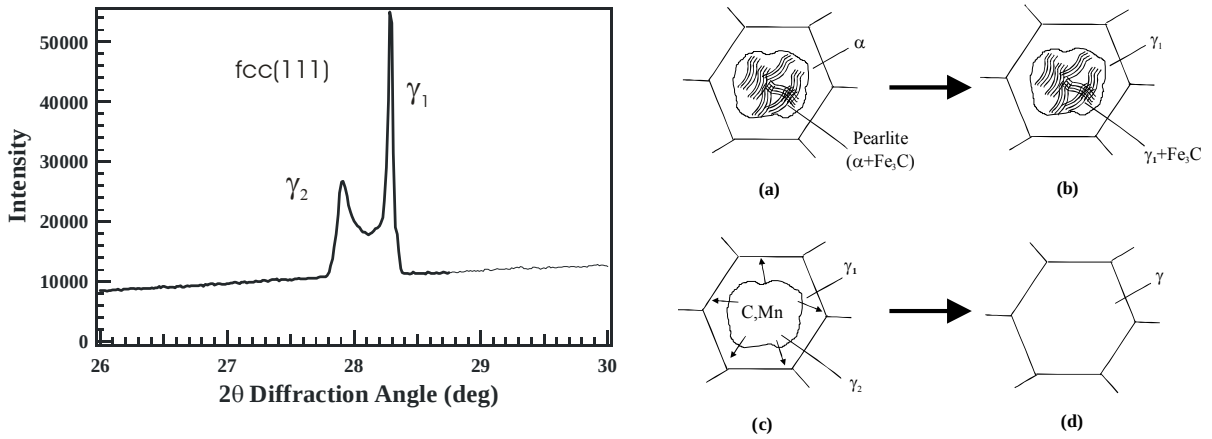

Figure 4: X-ray diffraction pattern taken showing splitting the fcc(111) austenite peak. Schematic diagrams showing the progression of the α→γ transformation.

Dynamic Observations of the α→γ Transformation using TRXRD. The TRXRD technique was used to investigate phase transformations in the 1045 steel at a single location in the weld HAZ located 5 mm from the center of the weld [18]. The TRXRD x-ray diffraction data for one of these runs is shown in Fig. 5a, which represents a series of 400 diffraction patterns, taken in 100 ms intervals, where welding time increases along the y-axis and the 2θ diffraction angle

increases along the x-axis. In this figure, the baseline diffraction data is shown for several seconds before the arc was turned on. After arc initiation, the arc was held on for 17s during heating, and for an additional 20s (after the arc was extinguished) to capture the cooling cycle. The higher diffraction peak intensity is indicated by the light tones, and lower peak intensities are indicated by dark tones, so that the diffraction peaks appear as streaks along the time axis at their appropriate 2θ locations.

At the beginning of the experiment (t=0), only three diffraction peaks exist, corresponding to the bcc phase. After the arc is turned on, these three bcc peaks rapidly shift to lower 2θ values as the crystal lattice of the steel expands during heating. With continued heating, three new peaks, corresponding to the fcc phase, appear. All six peaks coexisted for several seconds before the bcc peaks began to fade in intensity and disappear, leaving only the fcc diffraction peaks. The fcc peaks are then stable until the arc is extinguished at t=17s, after which the fcc peaks rapidly shift to higher 2θ values as the lattice contracts with cooling. With an additional 1.5 s of cooling, the bcc peaks reappear, and increase in intensity as the weld continues to cool.

Using the data presented in Fig. 5a, the relative fraction of the bcc and fcc phases present throughout both the heating and cooling cycles of the weld were determined. These data, based on measurements of the areas of the x-ray diffraction peaks are plotted in Fig. 5b as a function of time. The kinetics of the phase transformations can be determined from these plots as discussed in [11, 18].

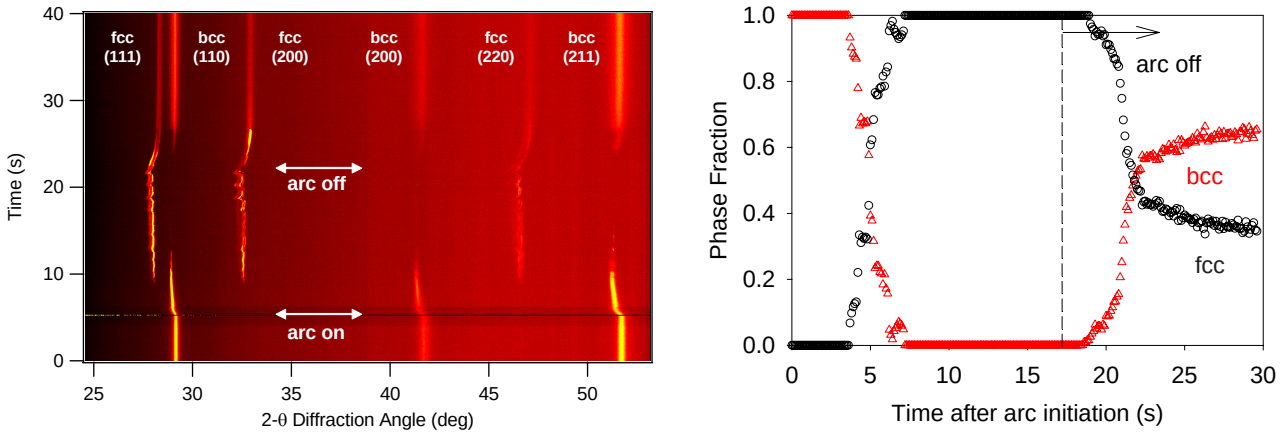

Fig. 5: a) TRXRD results showing the changes in the diffraction peaks as a function of welding time. b) Fraction of the bcc and fcc phases as a function of welding time in 1045 steel from (a).

Bainite and Martensite Formation During Rapid Cooling. In addition to measuring the fcc and bcc phases, additional information is provided in the x-ray diffraction peaks that can indicate the presence on nonequilibrium phases such as bainite and martensite. A closer look at the data presented in Fig. 5a reveals details about these phase transformation mechanisms during cooling, and Fig. 6a zooms in on the fcc(111) and bcc(110) peaks after the arc is extinguished. Initially, the fcc(111) peak rapidly shifts to higher 2θ values as the lattice contracts during cooling. Note that the fcc(111) peak is split, due to insufficient time for homogenization of austenite during the rapid TRXRD run. At t=23s, the bcc(110) peak first appears during cooling and has a relatively narrow peak width. Both peaks shift to higher 2θ values with continued cooling, and the bcc peak increases in intensity while the fcc peak decreases in intensity. At t=27s in this plot, both the bcc(110) and the fcc(111) peaks show a sudden increase in width. The wider bcc(110) peak exists throughout the remainder of the weld, increasing in intensity as the weld continues to cool. The sudden increase in peak width in the 1045 steel is caused by strain in the lattice as martensite forms.

The TRXRD diffraction peaks from above were analyzed to determine the relative fractions of the phases and their lattice parameters during weld cooling [18]. These results are plotted Fig. 6b, where the fraction bcc phase is shown on the left axis as the black circles, while the bcc lattice parameter is plotted on the right axis as the solid red triangles. In this figure, the first bcc phase appears at t=0.5s after the arc was extinguished. The initial rate of increase in the bcc phase is relatively slow, reaching approximately 15% transformed at t=2.8s. At this time, the bcc peaks rapidly increase in width, leading to a more than 2 times increase in the transformation rate, indicating that there is a change in the transformation mechanism as martensite forms. Fig. 6b also plots the measured lattice parameters during weld cooling. A decrease in the bcc lattice parameter is observed during the initial stages of transformation leading up to the change in mechanism at t=2.8s. This behavior would be expected if the initial stage of transformation was occurring by the formation of bainite since its lattice parameter would decrease as the weld cools. At t=2.8s, when the transformation rate increases, there is an increase in the lattice parameter from 2.906 to 2.908 Å. This increase in lattice parameter is caused by the formation of martensite.

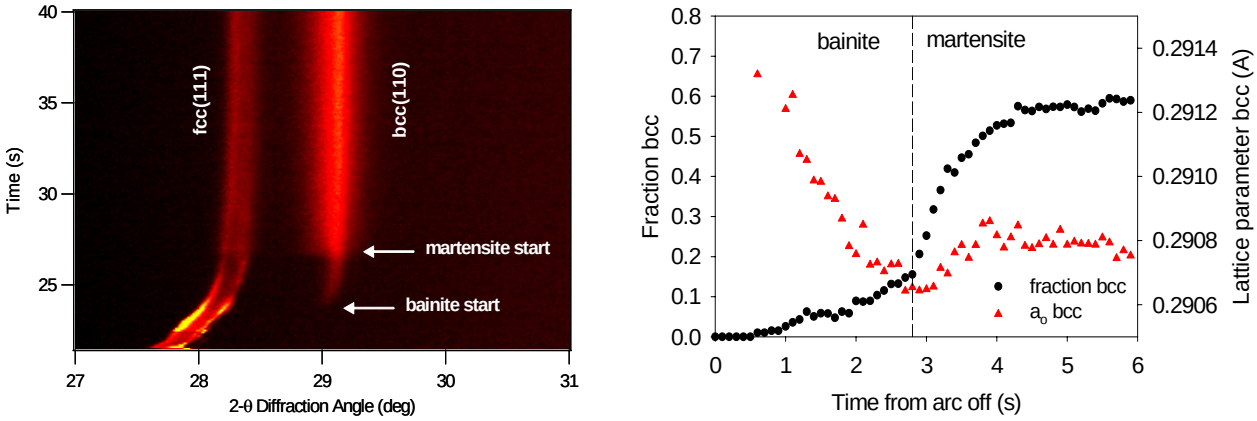

Figure 6. a) TRXRD results showing the fcc(111) and bcc(110) diffraction peaks during weld cooling. Martensite formation is accompanied by an increase in peak width. b) bcc fraction and lattice parameter as a function of weld cooling time. The transition from bainite to martensite occurs at t=2.8 after the arc was extinguished.

Microstructures of the 1045 steel are shown in Fig, 7. In the as received condition, Fig. 7a, the microstructure contains allotriomorphic ferrite and pearlite. The ferrite is the light etching phase that outlines the prior austenite grain boundaries, and the pearlite is the dark etching component within. Fig. 7b shows the microstructure of the HAZ at the location where the TRXRD data were obtained in the 1045 steel spot weld. In this microstructure, the prior austenite grain boundaries in the weld HAZ are much smaller than those in the original base metal as a result of the numerous nucleation sites provided within the original pearlite microstructure. No pearlite is present, and grain boundary ferrite is minimal. The bainitic portions of the microstructure appear as the darker etching patches located at the prior austenite grain boundaries. Within the grains, the microstructure is highly refined, and is characteristic of lath martensite that forms during rapid cooling of medium carbon steels. Therefore, the TRXRD results were able to distinguish between martensite and bainite phases based on their transformation rates, lattice parameters, and temperatures at which transformations initiated.

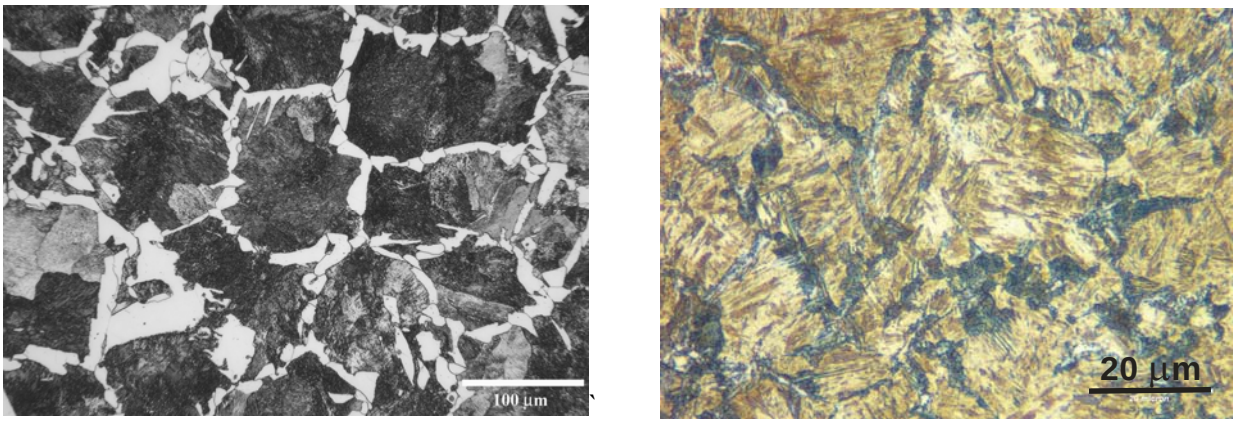

Figure 7: Microstructure of the 1045 steel in a) the as received condition, and b) after rapid cooling during the TRXRD experiment.

Conclusions

Synchrotron based x-ray diffraction techniques provide a powerful new tool for the study of phase transformations and microstructural evolution during welding. Through several examples of the application of SRXRD and TRXRD methods to 1045 steel, it can be seen that these unique experimental tools provide a number of capabilities not previously available to the welding researcher. When combined with additional experiments and modeling, these techniques allow a deeper understanding of the kinetics of phase transformations occurring in the weld metal and HAZ to be gained. As these techniques gain more widespread use, SRXRD and TRXRD will provide the welding research community with the ability to quantitatively describe the kinetics of other prominent phase transformations, and improve the knowledge base for the welding of steels and other alloys.

Acknowledgments

This work was performed under the auspices of the U. S. Department of Energy by UC, Lawrence Livermore National Lab. under Contract W-7405-ENG-48. This work was supported by DOE, Office of Basic Energy Sciences, Division of Materials Science. Portions of this research were carried out at the Stanford Synchrotron Radiation Laboratory, a national user facility operated by Stanford University on behalf of the U.S. Department of Energy, Office of Basic Energy Sciences. The authors would like to express their gratitude to Suresh Babu of the Edison Welding Institute, who provided Igor Pro® macros for the analysis of the x-ray data, and Mr. Bob Vallier of LLNL for performing the metallographic characterization of the base metal and welded samples.

References

1. Synchrotron Radiation Sources, A Primer: Edited by H. Winick, Stanford Synchrotron Radiation Laboratory, World Scientific Publishing Company, 1995.
2. J. W. Elmer, T. A. Palmer and S. S. Babu, "A New Experimental Method for In-Situ Phase Transformation Studies of Steels Using Synchrotron Radiation," *Advanced Materials and Processes*, V160(11), pp. 23-26, 2002.
3. J. W. Elmer, Joe Wong and Thorsten Ressler, "Spatially Resolved X-Ray Diffraction Mapping of Phase Transformations in the HAZ of C-Mn Steel Arc Welds," *Metall. and Mater. Trans. A*, 32A (5), pp. 1175-1187, 2001.
4. J. W. Elmer and T. A. Palmer, "In-Situ Mapping and Direct Observations of Phase Transformations During Arc Welding of 1045 Steel," submitted to *Metallurgical and Materials Transactions A*, September, 2005.

5. T. A. Palmer and J. W. Elmer, "Direct Observations of the $\alpha \rightarrow \gamma$ Transformation at Different Input Powers in the Heat Affected Zone of 1045 C-Mn Steel Arc Welds Observed by Spatially Resolved X-Ray Diffraction," in press *Metallurgical and Materials Transactions A*, June, 2005.
6. T. A. Palmer and J. W. Elmer, "Direct Observations of the Nucleation and Growth of Austenite from Pearlite and Allotriomorphic Ferrite in a C-Mn Steel Arc Weld," *Scripta Materialia*, V53(5), pp 535-540, 2005.
7. S. S. Babu, J. W. Elmer, S. A. David and M. Quintana, "In-Situ Observations of Non-equilibrium Austenite Formation During Weld Solidification of a Fe-C-Al-Mn Low Alloy Steel," *Proceedings of the Royal Society: Mathematical, Physical and Engineering Sciences*, 458, pp 811-821, 2002.
8. S. S. Babu, J. W. Elmer, J. M. Vitek, S. A. David, "Time-Resolved X-Ray Diffraction Investigation of Primary Weld Solidification in Fe-C-Al-Mn Steel Welds," *Acta Materialia*, Vol. 50, Iss. 19, pp 4763-4781, 2002.
9. T. A. Palmer, J. W. Elmer, and Joe Wong, "In-Situ Observations of Ferrite/Austenite Transformations in Duplex Stainless Steel Weldments Using Synchrotron Radiation," *Science and Technology of Welding and Joining*, 7(3), pp 159-171, 2002.
10. J. W. Elmer, T. A. Palmer and Joe Wong, "In-Situ Observations of Phase Transitions in Ti-6Al-4V Alloy Welds using Spatially Resolved X-Ray Diffraction," *Journal of Applied Physics*, V93(4), pp1941-1947, 15 Feb., 2003.
11. T. A. Palmer, J. W. Elmer, S. S. Babu, "Observations of Ferrite/Austenite Transformations in the Heat Affected Zone of 2205 Duplex Stainless Steel Spot Welds Using Time Resolved X-Ray Diffraction." *Materials Science and Engineering A*, Vol. 374, pp. 307-321, 2004.
12. J. W. Elmer, Joe Wong and Thorsten Ressler, "In-Situ Observations of Phase Transformations During Solidification and Cooling of Austenitic Stainless Steel Welds using Time-Resolved X-Ray Diffraction," *Scripta Materialia*, 43(8), pp. 751-757, 2000.
13. Z. Yang, J. W. Elmer, Joe Wong, and T. DebRoy, "Evolution of Titanium Arc Weldment Macro- and Microstructures – Modeling and Real Time Mapping of Phases," *Welding Journal*, 79(4), p. 97s-112s, 2000.
14. J. W. Elmer, T. A. Palmer, W. Zhang, B. Wood, and T. DebRoy, "Kinetic Modeling of Phase Transformations Occurring in the HAZ of C-Mn Steel Welds Based on Direct Observations," *Acta Materialia*, V51, pp. 3333-3349, 2003.
15. W. Zhang, J. W. Elmer, and T. DebRoy, "Modeling and Real Time Mapping of Phases during GTA Welding of 1005 Steel," *Materials Science and Engineering A*, v 333, issue 1-2, pp 321-335, 2002.
16. W. Zhang, G. G. Roy, J. W. Elmer, and T. DebRoy, "Modeling of Heat Transfer and Fluid Flow during GTA Spot Welding of 1005 Steel," *Journal of Applied Physics*, V93(5), pp. 3022-3033, 1 Mar., 2003.
17. W. Zhang, J. W. Elmer, and T. Debroy, "Integrated Modeling of Thermal Cycles, austenite formation, grain growth and decomposition in the heat affected zone of carbon steel," *Science and Technology of Welding and Joining*, V10(5), pp 574-582, 2005.
18. J. W. Elmer, T. A. Palmer, S. S. Babu, W. Zhang and T. Debroy, "Direct Observations of Austenite, Bainite, and Martensite Formation During Arc Welding of 1045 Steel using Time Resolved X-ray Diffraction," *Welding Journal*, V83(9), pp 244-s to 253-s, 2004.
19. K. Mundra, T. DebRoy, and K. Kelkar, *Numerical Heat Transfer*, (29), pp. 115-129, 1996.
20. K. Mundra, J.M. Blackburn, and T. DebRoy, *Sci. Technol. Welding Joining*, 2(4), pp. 174-184, 1997.
21. B. Sundman, B. Jansson and J. Andersson, *Calphad-Computer Coupling of Phase Diagrams and Thermochemistry*, V 9(2), p.153, 1985.